The role of frictional strength on plate coupling at the subduction interface

Eh Tan

Institute for Geophysics, Jackson School of Geosciences, University of Texas at Austin, 10100 Burnet Road, Austin, Texas 78758, USA

Now at Institute of Earth Sciences, Academia Sinica, Taipei 11529, Taiwan (tan2@earth.sinica.edu.tw)

Luc L. Lavier

Institute for Geophysics, Jackson School of Geosciences, University of Texas at Austin, 10100 Burnet Road, Austin, Texas 78758, USA

Department of Geological Sciences, Jackson School of Geosciences, University of Texas at Austin, Austin, Texas 78712, USA

Harm J. A. Van Avendonk

Institute for Geophysics, Jackson School of Geosciences, University of Texas at Austin, 10100 Burnet Road, Austin, Texas 78758, USA

Arnauld Heuret

Dipartimento di Scienze Geologiche, Università degli Studi "Roma Tre", IT-00146 Rome, Italy

Now at Laboratoire de Recherche en Géosciences, Université des Antilles et de la Guyane, Campus de Fouillole, FR-97159 Pointe-à-Pitre Cedex Guadeloupe (FWI), France

[1] At a subduction zone the amount of friction between the incoming plate and the forearc is an important factor in controlling the dip angle of subduction and the structure of the forearc. In this paper, we investigate the role of the frictional strength of sediments and of the serpentinized peridotite on the evolution of convergent margins. In numerical models, we vary thickness of a serpentinized layer in the mantle wedge (15 to 25 km) and the frictional strength of both the sediments and serpentinized mantle (friction angle 1° to 15°, or static friction coefficient 0.017 to 0.27) to control the amount of frictional coupling between the plates. With plastic strain weakening in the lithosphere, our numerical models can attain stable subduction geometry over millions of years. We find that the frictional strength of the sediments and serpentinized peridotite exerts the largest control on the dip angle of the subduction interface at seismogenic depths. In the case of low sediment and serpentinite friction, the subduction interface has a shallow dip, while the subduction zone develops an accretionary prism, a broad forearc high, a deep forearc basin, and a shallow trench. In the high friction case, the subduction interface is steep, the trench is deeper, and the accretionary prism, forearc high and basin are all absent. The resultant free-air gravity and topographic signature of these subduction zone models are consistent with observations. We believe that the low-friction model produces a geometry and forearc structure similar to that of accretionary margins. Conversely, models with high friction angles in sediments and serpentinite develop characteristics of an erosional convergent margin. We find that the strength of the subduction interface is critical in controlling the amount of coupling at the seismogenic zone and perhaps ultimately the size of the largest earthquakes at subduction zones.

1. Introduction

[2] The subduction of an oceanic plate beneath an overriding continental or oceanic plate is primarily driven by slab pull. The corresponding cooling and contraction of the descending oceanic lithosphere, as well as the density increase caused by prograde metamorphic reactions at depth, provide a consistent driving force for subduction. Slab pull is counteracted to some degree by frictional resistance between the two plates. This leads to the periodic accumulation of elastic stresses at the interface between the plates that are episodically released in large earthquakes. Hence, this interface is called the seismogenic zone over the depth range where unstable slip occurs. The upper limit of the seismogenic zone may coincide with compaction and diagenesis of sediments or cementation, consolidation or strain dependent slip localization in the accretionary prism [*Moore and Saffer*, 2001; *Saffer and Marone*, 2003], whereas the deeper limit is thought to be controlled by the temperature at which rocks transition from brittle to ductile behavior [*Oleskevich et al.*, 1999; *Schwartz and Rokosky*, 2007]. A worldwide compilation shows that the seismogenic zone often lies between 10 km and 50 km depth, and that the dip angle θ varies between 10° and 35° [*Heuret et al.*, 2011].

[3] The amount of friction between the downgoing and overriding plates may be an important factor in controlling the dip angle θ, and structure of the forearc region. For example, critical wedge theory for frictional materials [*Davis et al.*, 1983; *Dahlen et al.*, 1984] predicts that the frontal wedge angle is dependent on the static friction coefficient μ at the subduction interface. Wedge theory predicts that a low friction coefficient on the thrust interface generates a shallow accretionary wedge, whereas high friction between the plates produces a steep wedge. Critical wedge theory is successful in this setting because it is realistic to assume the Mohr-Coulomb failure criterion for sediments. However, when applied to the deeper lithosphere it fails to

address viscous and elastic properties of the Earth. For a subducting elastic plate, the dip angle at the depth of the seismogenic zone may result from a balance between the elastic bending moment and the frictional and viscous resistance to subduction.

[4] The frictional strength of a material is determined by the friction angle ϕ, or by the static friction coefficient $\mu = \tan\phi$. *Byerlee* [1978], gathering data from a wide range of rock types, showed that the static friction coefficient does not vary very much at pressures above 200 MPa, where it is on the order of 0.6 ($\phi \approx 30°$). However, *Byerlee* [1978] qualifies that observation with the important caveat that minerals populating fault gouges could have very low friction coefficients. The friction angles of minerals populating the fault gouges, such as clay, quartz and phyllosilicates (talc and smectite) as well as those of granite, sedimentary rocks and serpentinized peridotites have been estimated in laboratory experiments [*Blanpied et al.*, 1995; *Moore et al.*, 1997; 2004; *Saffer and Marone*, 2003, *Collettini et al.*, 2009; *Lockner et al.*, 2011; *Faulkner et al.*, 2011; *Saffer et al.*, 2012] at low and high strain rates, and for both dry and wet conditions (Table 1). The data presented here are not exhaustive but demonstrate the fact that the friction coefficient at the subduction interface can span a wide range of values and could potentially vary spatially over the depth of the seismogenic zone depending on the composition of fault gouges. The lowest value in Table 1 corresponds to smectite (0.07) and the largest to granite (0.8) corresponds to a range of friction angles of 4° to 38°.

[5] Numerical studies of subduction often assume a very weak shear zone with a strength on the very low end of the values in Table 1. The resultant models can maintain motion at the subduction interface [e.g., *Hassani et al.*, 1997; *Hall et al.*, 2003; *Gurnis et al.*, 2004; *Gorczyk et al.*, 2007; *Kaus et al.*, 2008; *Faccenda et al.*, 2009; *van Dinther et al.*, 2012] with a friction coefficient between 0.01 and 0.1 (friction angle of 0.5° to

Table 1. The Values Presented Here Correspond to Friction Coefficients Estimated at Both Low and High Strain Rates and in Dry and Wet Conditions for Different Pressure and Temperature Conditions Corresponding to the Seismogenic Zone

	Friction Coefficient	
	Dry	Wet
Granite gouges [*Blanpied et al.*, 1995]	0.7–0.8	0.5–0.7
Clay rich gouges [*Saffer and Marone*, 2003, and references therein]	Smectite 0.07–0.3	0.13–0.3
	Smectite+Quartz 0.2–0.53	
	Illite 0.41–0.63	
Marine mudstones [*Saffer et al.*, 2012]	Clay rich 0.24–0.4	N/A
Clay rich material [*Faulkner et al.*, 2011]	0.1–0.6	0.09–0.24
Foliated fault zone [*Collettini et al.*, 2009]	Talc-Smectite 0.24–0.47	N/A
Serpentinite gouge [*Moore et al.*, 1997; *Moore et al.*, 2004]	0.6–0.7	0.1–0.5

5.7°). Most studies assume that the effective friction coefficient at the subduction interface is lower by the presence of pore fluid. Such a low friction coefficient often allows for a very strong oceanic lithospheric plate to pass through a subduction zone. Alternatively, it is very likely that bending and fracturing of the downgoing plate near the trench decreases the bending resistance and moment, which will also facilitate subduction. Seismological evidence for fracturation and weakening by serpentinization in the bending downgoing plate exists along several convergent margins [e.g., *Van Avendonk et al.*, 2011]. Using a numerical model of subduction, *Faccenda et al.* [2009] also showed how bend-faulting in the descending plate can lead to serpentinization in the oceanic mantle. Moreover, *Buffett and Becker* [2012] showed that the characteristic geometry of the world's trench-forearc systems is best explained by a deformed and plastically weakened downgoing plate. If the bending moment in the downgoing plate is reduced during subduction such as some observations suggest [*Buffett and Becker*, 2012], the friction angle at the subduction interface may not have to be so low as assumed in previous numerical studies. In this study we investigate whether the range of friction angles from 8° to 26° observed in wet fault gouges in laboratory experiments (Table 1) may be representative for a subduction plate interface.

[6] We use a dynamic model that takes into account the elastic, plastic, viscous and frictional properties of the lithospheric plates to investigate how the structure of the forearc region and the strength of the subduction interface interact to develop a steady state geometry over millions of years. We present numerical models that explore the role of the

frictional strength of subducting sediments, the frictional strength and thickness of the serpentinized peridotite layer in the mantle wedge in the evolution of subduction zones. We find that the friction angle ϕ affects the dip angle θ of the subduction interface, and the structure and gravity signature of the forearc. Finally, we discuss whether the long-term strength of the forearc region could be used as an indicator of seismicity.

2. Geophysical Observations

[7] The structure of accretionary prisms and underlying oceanic crust has been imaged in great detail along 2-D marine seismic reflection and refraction profiles. Seismic reflection images show how incoming sediments are compacted, dewatered, and deformed as they underthrust or accrete to the prism [*Bangs et al.*, 2004; *McIntosh et al.*, 2007; *Gulick et al.*, 2011]. Deeper beneath the forearc, the dip of the subducting plate interface θ may be defined by wide-angle seismic reflections from the downgoing oceanic basement [*Kodaira et al.*, 1996; *Holbrook et al.*, 1999; *Sallarès and Ranero*, 2005], and by the depth of earthquakes in the seismogenic zone [*Pacheco et al.*, 1993; *Heuret et al.*, 2011].

[8] Seismic reflection and refraction data show that the size of accretionary prisms varies widely between different subduction zones (Figure 1). For example, the sediment cover on the forearc block of the central Aleutians appears to be just a few kilometers thick [*Holbrook et al.*, 1999], but in Sumatra the thickness of the accreted sediments exceeds 10 km [*Klingelhoefer et al.*, 2010]. This disparity is not surprising, given that the sediment input from
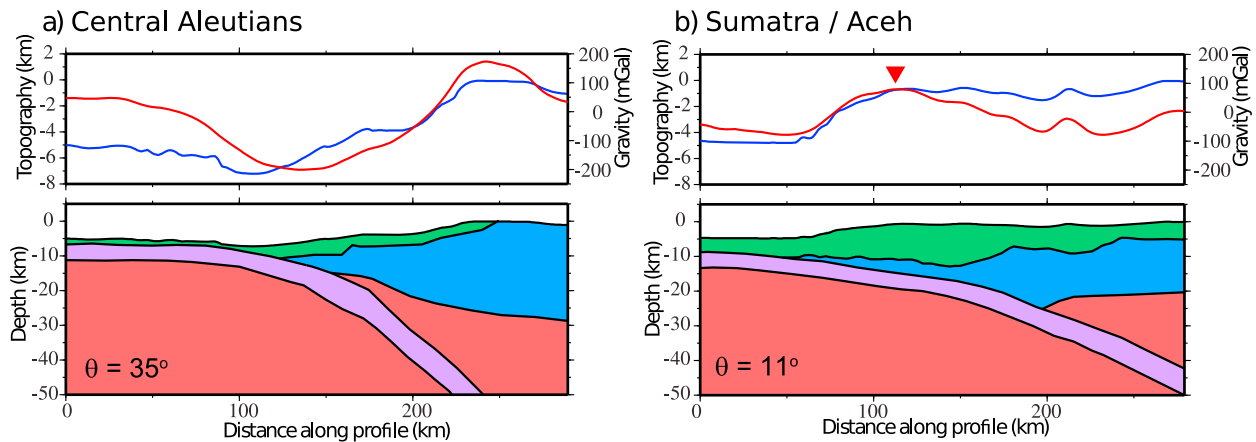
Figure 1. Large-scale structure of the subduction zones of (a) the Central Aleutians (modified from *Holbrook et al.* [1999]) and (b) Sumatra (modified from *Klingelhoefer et al.* [2010]) inferred from active-source seismic data. The upper panels show the model topography (blue lines) [*Smith and Sandwell*, 1997], the free air gravity anomaly (red lines) [*Sandwell and Smith*, 2009] along these two seismic profiles. The red triangle marks the positive gravity anomaly in the forearc. The fields in the lower panels represent inferred mantle (red), upper plate crystalline crust (blue), lower plate crystalline crust (purple), and sediments (green). We here assume that the boundary between accreted sediments and forearc basement largely coincides with the 5.5 km/s contour and the Moho at 7.5 km/s contour in these seismic images.

incoming plates is equally variable, and the fraction of subducted versus accreted sediments also differs between convergent margins [*von Huene and Scholl*, 1993; *Clift and Vannucchi*, 2004]. Sediment subduction probably helps to protect the overlying basement from tectonic erosion [*von Huene and Ranero*, 2009], so the sediment supply has a strong influence on the forearc crustal structure as well.

[9] Though the Alaskan-Aleutian subduction has sometimes been characterized as an accreting margin in global compilations [*von Huene and Scholl*, 1991; *Clift and Vannucchi*, 2004], there is clearly a strong along-strike variation in the sediment supply and the style of subduction at this plate boundary [*Scholl and von Huene*, 2007; *Bilek*, 2010]. Offshore southern Alaska, the landward sediment influx is very large, resulting in a growing prism [*Moore et al.*, 1991; *Worthington et al.*, 2010]. To the west, the sediment prism on the eastern and central Aleutian trench is much smaller, and a seaward decrease in forearc crustal seismic velocities is indicative of tectonic erosion [*Holbrook et al.*, 1999; *Lizarralde et al.*, 2002]. We therefore use the central Aleutian convergent margin [*Holbrook et al.*, 1999] as a typical example of an erosional margin where the forearc basement rock is carried along the subduction interface into the deeper mantle.

[10] Sumatra is a good example of an accretionary margin, where a large amount of sediments is added to the upper plate [*Chauhan et al.*, 2009; *Klingelhoefer et al.*, 2010]. The structural difference between the

central Aleutians and Sumatra forearc regions (Figure 1) is characterized by a very shallow dip angle θ of subduction interface in Sumatra (11°) and a rather steep θ in the central Aleutians (25°). In addition, the topographic (blue) and free-air gravity anomaly profiles (red) are also very different between these two margins (Figure 1). In the central Aleutians (Figure 1a) the basement climbs steeply from a large depth (>~12 km) at the trench to a high near sea level over a distance of about 100 km. The corresponding gravity profile (red) shows a characteristic trench low of −200 mGal to a forearc bulge of about 180 mGal. In Sumatra (Figure 1b), the top of basement has a very shallow slope over a distance of 150 km. The basement forms a broad forearc high adjacent to a 4-km-deep forearc basin. The gravity anomaly across the Sumatra convergent margin shows less variation in amplitude than in the Aleutians, −80 to 100 mGal from the trench to the top of the accretionary prism, and it has a high in the forearc (red triangle in Figure 1b) that does not correspond to interpreted basement depth nor Moho depth. The comparison of the central Aleutians and Sumatra, which may be considered representative as the sediment-starved and sediment-rich end-members among convergent margins, illustrates that sediment supply has a great influence on the deeper structure and geometry of subduction zones.

[11] The amount of stress coupling between the downgoing and overriding plates depends on the thickness and the frictional strength of the subducting

sediment layer. A thick, but strong, sediment layer would exert similar degree of stress coupling on the subduction interface as a thin, but weak, sediment layer would. Likewise, a sediment-rich subduction zone would, in general, have weaker subduction interface than a sediment-poor subduction zone. We would expect that a numerical model with small friction angle of the sediment would share the characteristics of a sediment-rich subduction zone, such as the Sumatra, and a model with high friction angle share the characteristics of a sediment-poor subduction zone, such as the central Aleutians.

[12] Over the last decade, high-quality earthquake seismic data have helped to image the structure of the plate interface and the mantle wedge beneath the arc and forearc, providing unprecedented constraints on strain patterns and material transfers in the subduction system Tomographic seismic velocity models show that the outer wedge of many subduction zones may consist of relatively cool, serpentinized mantle material that is stagnant, whereas the rest of the mantle wedge is engaged in corner flow [*Yamamoto et al.*, 2011]. Receiver function analyses [*Tibi et al.*, 2008; *Nikulin et al.*, 2009; *Sodoudi et al.*, 2011] and seismic waveguide studies [*Abers*, 2005] have also found evidence of a distinct low seismic velocity layer on top of the downgoing oceanic plates in the mantle wedge. This boundary layer may be the result of hydration by fluids rising from the subducting slab, which could locally lead to serpentinization [*Ulmer and Trommsdorff*, 1995] or mantle melting [*Schmidt and Poli*, 1998], depending on the pressure and temperature conditions in the wedge.

[13] Besides the strength and thickness of incoming sediments, another factor that may control the subduction dip angle is the strength of the serpentinized mantle wedge. Even weakly serpentinized peridotite has a low friction angle ϕ of 17°, which corresponds to a friction coefficient μ of 0.3 [*Escartín et al.*, 2001; *Hilairet et al.*, 2007], so it likely reduces friction at the subduction interface, in the same way that the presence of sediments would. The in situ friction coefficient of the sediment and serpentinized peridotite is not well constrained from lab experiments. The possible presence of pore fluid would decrease the effective friction coefficient further at the subduction interface at a wide range of depths [e.g., *Moore et al.*, 1995; *Wada et al.*, 2008; *Audet et al.*, 2009; *Van Avendonk et al.*, 2010]. In our geodynamic models we will assume that the friction angle ϕ of the sediments and that of serpentine vary similarly, and we will vary ϕ as a controlling parameter. The base

friction coefficient of compacted sediments and serpentinized peridotite are indeed comparable (~0.3) [*Kirby and Kronenberg*, 1987; *Hilairet et al.*, 2007]. Another ill-constrained parameter is the thickness of serpentinized peridotite in the mantle wedge. From seismic tomography we can obtain estimates of fluid content in the mantle wedge [*Carlson and Miller*, 2003; *Syracuse et al.*, 2008], but observations of the detailed structure above the plate boundary are relatively sparse [*Nikulin et al.*, 2009]. Therefore, we will treat the vertical extent of the serpentinized peridotite as another controlling parameter in the models.

[14] Many scientists have used global compilations to relate the subduction dip angle to other geometric parameters and physical properties of subduction zones [*Jarrard*, 1986; *Lallemand et al.*, 2005; *Heuret et al.*, 2011]. *Heuret et al.* [2011] correlate physical parameters characterizing the geometry, the plate velocities and the stress state of the subduction zone. They generally show that there is some correlation between the dip of the subduction interface and the convergence rate, though the correlation coefficient only ranges between 0.5 and 0.6, depending on the frame of reference. A lower correlation coefficient is found between dip angle and incoming plate age. Using a global compilation of sediment thickness data [*Heuret et al.*, 2012] we find that there is a better correlation between the dip of the seismogenic subduction interface θ (Figure 2a) and sediment thickness (Figure 2b). Analyzing the data in details we find that the sediment thickness is inversely proportional to θ with a correlation coefficient of 0.65. If we exclude the western Aegean trench from the fit, which is a clear outlier, the correlation coefficient is 0.70 (Figure 2c). *Song and Simons* [2003] and *Heuret et al.* [2012] showed that there is a relationship between the topography of the forearc region, the sediment thickness at the trench, and the generation of mega-earthquakes. These observations strongly motivate our choice to investigate the possible relationship between the sediment thickness, sediment strength, and the dip of the seismogenic interface.

3. Numerical Methods

[15] We use numerical and rheological approximations of the thermomechanical processes occurring in the lithosphere to model the effects of friction on the subduction interface. Our numerical code uses the *Fast Lagrangian Analysis of Continua* (FLAC)
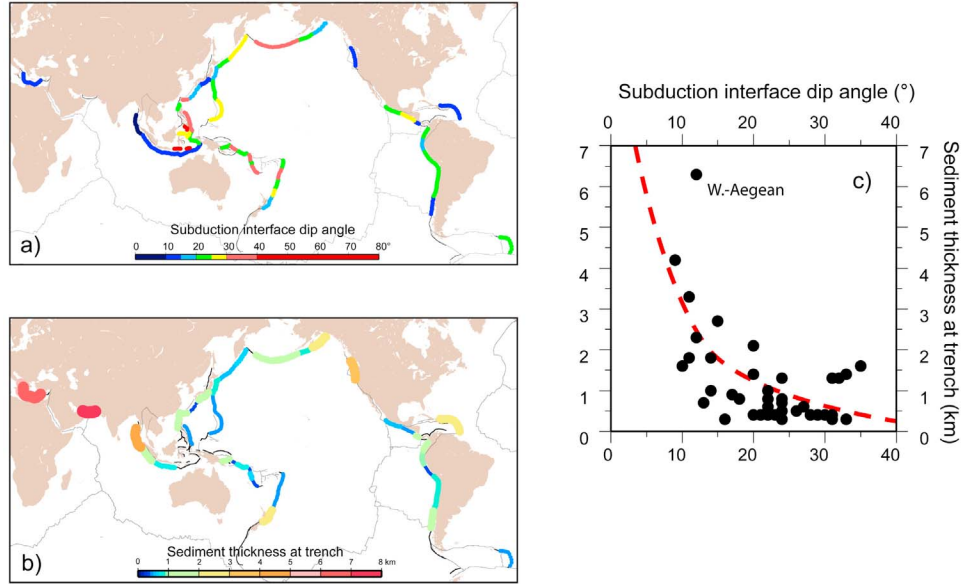
Figure 2. (a) Map of the distribution of dip angle at subduction interface worldwide [*Heuret et al.*, 2011]. (b) Map of the distribution of sediment thicknesses at trenches worldwide [*Heuret et al.*, 2012]. (c) Plot of dip angle θ versus sediment thickness. When correlated inversely with dip angle, the coefficient of correlation for sediment thickness is 0.65. If the W. Aegean trench is excluded from the fit, the coefficient of correlation becomes 0.70.

technique [*Cundall*, 1989]. The detailed algorithm is presented elsewhere [*Poliakov et al.*, 1993; *Lavier et al.*, 2000] and will be only briefly described here. The equation of motion with elasto-visco-plastic rheology is solved explicitly on a finite element, Lagrangian grid. The elastic wave is strongly damped to achieve quasi-static equilibrium. The stresses due to elasto-viscous and elasto-plastic flow are computed on each element. The lesser of the stress second invariants (effective stress) is taken as the final stress of the element. Linear elasticity is computed with the Lame parameters $\lambda_1 = \lambda_2 = 3 \times 10^{10}$ Pa. For plasticity, the shear stress at yield τ_y depends on the cohesion C, normal stress σ_n, and friction angle ϕ. The relationship is given by Mohr-Coulomb law:

$$\tau_y = C + \sigma_n \tan \phi. \tag{1}$$

Both the cohesion and friction angle are subjected to strain weakening and decrease linearly with the amount of plastic strain ε_{pl} up to their saturation values (Figure 3). The values used for cohesion and friction of the different materials are listed in Table 2. In all the models, serpentinized mantle and sediments strength can vary, all other lithospheric material are assumed to weaken frictionally from $\phi = 30°$ to $\phi = 15°$. The lower values correspond to an oceanic crust and mantle that are strongly weakened by brittle plastic deformation, and in which the elastic bending moment is strongly reduced.

[16] To calculate the viscosity we use dislocation creep laws from laboratory experiments (Table 2). The viscosity is nonlinear and depends on the second invariant of the strain rate $\dot{\varepsilon}_{II}$, the stress exponent n, the viscosity pre-exponent A, the activation energy E, the universal gas constant R, and the temperature T. The viscosity is expressed as [*Chen and Morgan*, 1990]:

$$\eta = \frac{1}{4}\left(\frac{4}{3A}\right)^{\frac{1}{n}} \dot{\varepsilon}_{II}^{\frac{1-n}{n}} \exp\left(\frac{E}{nR(T+273)}\right). \tag{2}$$

Though the viscosity can be lowered with temperature and strain, we impose a minimum cut-off
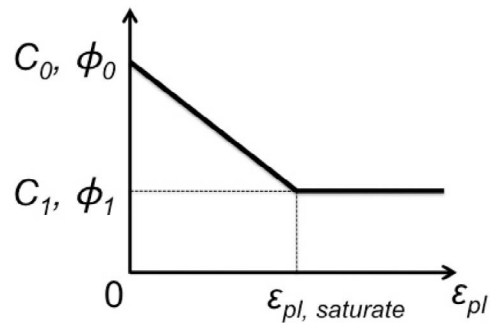
Figure 3. The cohesion and friction angle are C_0 and ϕ_0 when $\varepsilon_{pl} = 0$, and decrease linearly to C_1 and ϕ_1 when $\varepsilon_{pl} \leq \varepsilon_{pl,saturate} = 0.1$. Further plastic deformation will not affect cohesion and friction angle.

Table 2. Rock Parameters Used in the Models[a]

	Rock Type						
	Overriding Crust	Oceanic Crust, Basalt	Subducted Oceanic Crust, Eclogite	Mantle, Peridotite	Serpentinized Mantle Peridotite	Sediments	Dehydrated Sediments, Schist
Density (kg/m^3)	2900	2880	3480	3300	3200	2400–2800[b]	2900
n	3.05	3.05	3.05	3	3	3	3
A (MPa^{-n}s^{-1})	1.25×10^{-1}	1.25×10^{-1}	1.25×10^{-1}	7×10^4	7×10^4	5×10^2	7×10^4
E (J mol^{-1})	5.76×10^5	3.76×10^5	4.5×10^5	5.2×10^5	1.2×10^5	2×10^5	3.76×10^5
C_0 (Pa)	4×10^7	4×10^7	4×10^7	4×10^7	4×10^6	4×10^6	4×10^7
C_1 (Pa)	4×10^6	4×10^6	4×10^6	4×10^6	4×10^6	4×10^6	4×10^6
ϕ_0 (°)	30	30	30	30	varies	varies	30
ϕ_1 (°)	15	15	15	15	varies	varies	15

[a]References: *Ranalli* [1986]; *Kirby and Kronenberg* [1987]; *Chen and Morgan* [1990].
[b]The density of sediments increases linearly from 2400 kg/m^3 at the surface to 2800 kg/m^3 below 6 km depth due to compaction.

value. Setting the cut-off value to 10^{19} Pa·s will increase the flow velocity in the asthenosphere and slow down the computation, compared with a cut-off value 10^{20} Pa·s, while the deformation in the lithosphere is largely unaffected by the choice of the cut-off value. Therefore we will use 10^{20} Pa·s as the minimum cut-off for the viscosity. In terms of overall force balance, *Gurnis et al.* [2004] have shown that such viscosity is adequate since the viscous resistance in the asthenosphere becomes low enough so that it does not impact the force balance in the lithosphere.

[17] For all computations we define a starting model on a 960-km-wide and 300-km-thick rectangular grid that is divided in an oceanic and a continental plate portion (Figure 4). The oceanic crust is 7 km thick and is overlain by 0.5 km of sediment. The oceanic plate is 400 km long initially and has a thermal profile that corresponds to the 60-Myr half-space cooling model (Figure 4). The adjacent continental crust thickens from 7.5 km near the future convergent margin to 25 km at the right boundary. This 560 km long continental block has a geotherm with a thermal age that gradually
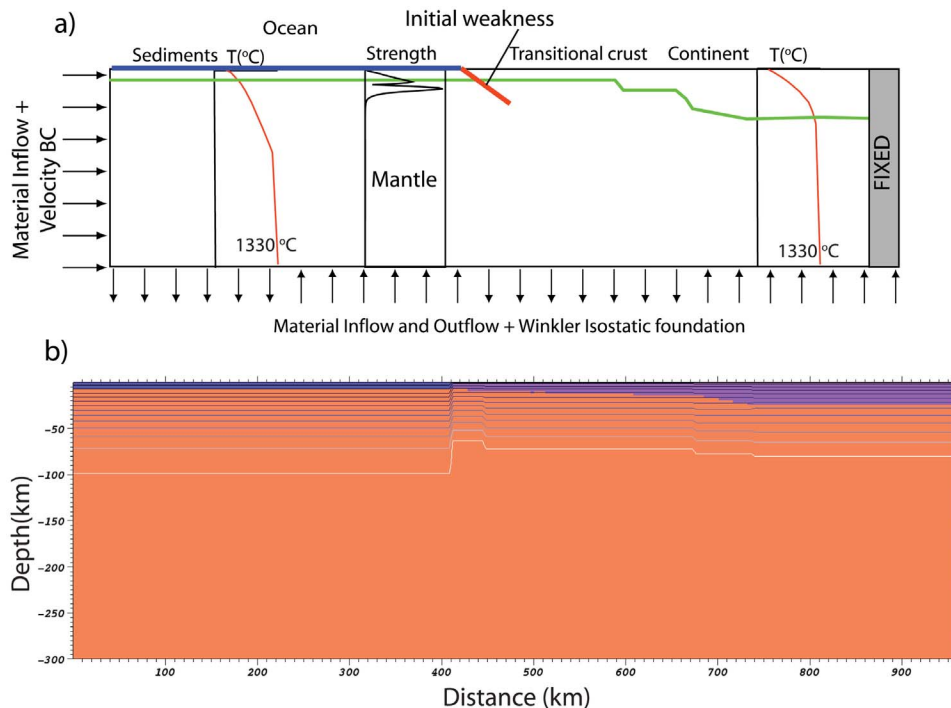
Figure 4. Initial conditions. (a) Schematic representation of the model initial and boundary conditions (not to scale). (b) Phases and temperature contours at 100°C intervals with the temperature being 1300°C at 100 km on the left side. In orange is mantle peridotite, in blue basaltic crust and in purple the upper plate crust.

increases from 30 Myr at the margin to 60 Myrs at the right boundary. An initial weak zone (pre-existing plastic failure) at the plate boundary extends from surface to 30 km depth with 18° dip angle. The grid spacing is refined near the surface and the middle of the domain, with the finest grid spacing 4 km in the x direction and 1.5 km in the z direction. Additionally, near one million markers (initially 9 per elements) are used to track material, which allow us to represent a sediment layer of 0.5 km thickness.

[18] We force the continent-ocean boundary into subduction zone by moving the oceanic (left) wall to the right at a constant speed 5 cm/yr, while the opposite right wall is pinned horizontally. We do not vary the boundary velocity between the different models since we believe that this parameter is not critical in controlling geometry at the subduction interface where material deformation is dominated by pressure dependent phenomena. At larger depth, where the slab is warmer and the mantle more viscous, this parameter is likely critical since deformation there is highly strain rate dependent, however our study is not focused on the slab dip deep in the mantle. Vertical motion along both walls is unconstrained. The top boundary has free surface. The model applies water loading for surface elements below sea level (0 m) and no loading above sea level. The bottom boundary is supported by an inviscid fluid and is open to outflow and inflow. When the elements become too distorted with ongoing deformation, a remeshing step restores the left and bottom model boundaries to the initial locations. The topography of the top surface is preserved during remeshing. The temperature is fixed at 0°C for the top surface, and at 1330°C for the bottom boundary. Erosion and sedimentation of surface topography is implemented with simple diffusion, with a low diffusion coefficient 10^{-6} m²/s. A new sediment marker is inserted to the element when sufficient sediment accumulates. We chose a low coefficient of diffusivity for the erosion and sediment processes because we cannot accurately account for sediment transport processes in a 2-D model.

[19] We use constant coefficient of thermal expansion (3×10^{-5} K⁻¹), thermal conductivity (3.0 W·m⁻¹·K⁻¹), and heat capacity (10^3 J·kg⁻¹·K⁻¹) for all materials. The effect of frictional heating, radiogenic heating, and plastic strain healing are also accounted in the computation, though their effects are small. The physical properties used in the models are compiled in Table 2.

[20] We used simplified phase diagrams to model the hydration-dehydration metamorphic reactions.

The oceanic crust will dehydrate to eclogite when temperature T and pressure P conditions satisfy two conditions [Hacker, 1996]:

$$\begin{array}{c} P > 2.2T - 300 \, (\text{MPa}) \\ T > 500 \, (°C) \end{array} \qquad (3)$$

Water released by dehydration of downgoing oceanic crust [Peacock, 1993] will hydrate a layer of the overlying mantle wedge. We do not include the thermodynamics and kinematics of mineral hydration nor the dynamics of porous flow. Instead, we parameterized the hydration process by instantaneously transforming the mantle peridotite to serpentinized peridotite up to a thickness H_{serp} above the subducted oceanic crust or sediments. Serpentine is known to have a very weak creep rheology [Hilairet et al., 2007] and a density of about 2400 kg·m⁻³. The amount of serpentinization in the mantle wedge is highly variable [e.g., Hyndman and Peacock, 2003]. We chose a conservative estimate in our model of 10 to 20% of serpentinization that is consistent with most subduction zones [Abers, 2005]. A small amount of serpentinized peridotite likely reduces the bulk creep strength of the mantle by a large amount [e.g., Handy, 1989]. To model serpentinized peridotite we therefore chose to decrease the activation energy of mantle peridotite from 5.2×10^5 to 1.2×10^5 J·mol⁻¹, which corresponds to a very weak mantle with minimum viscosity in our models. We decrease the density by 100 kg·m⁻³ that corresponds to about 15% of mantle serpentinization. The serpentinized peridotite can transform back to peridotite under higher P-T conditions [Ulmer and Trommsdorff, 1995]:

$$\begin{array}{c} P > \dfrac{5.4}{230(730 - T)} + 2.1 \, (\text{GPa}) \\ T > 550 \, (°C) \end{array} \qquad (4)$$

Likewise, the subducted sediments will turn into schist when temperature is greater than 650°C and pressure is greater than 600 MPa [Nichols et al., 1994].

4. Results

[21] We ran 15 cases and systematically changed the friction angle ϕ of the incoming sediments and serpentinized peridotite from 1°, 3°, 5°, 9° to 15°, while also changing the thickness H_{serp} of the serpentinite layer from 15 km, 20 km, to 25 km. In each case we computed 40 Myrs of model time until the subduction geometry becomes stable. We approximated the seismogenic zone as the portion of the mega-shear between the 100° and 400°C
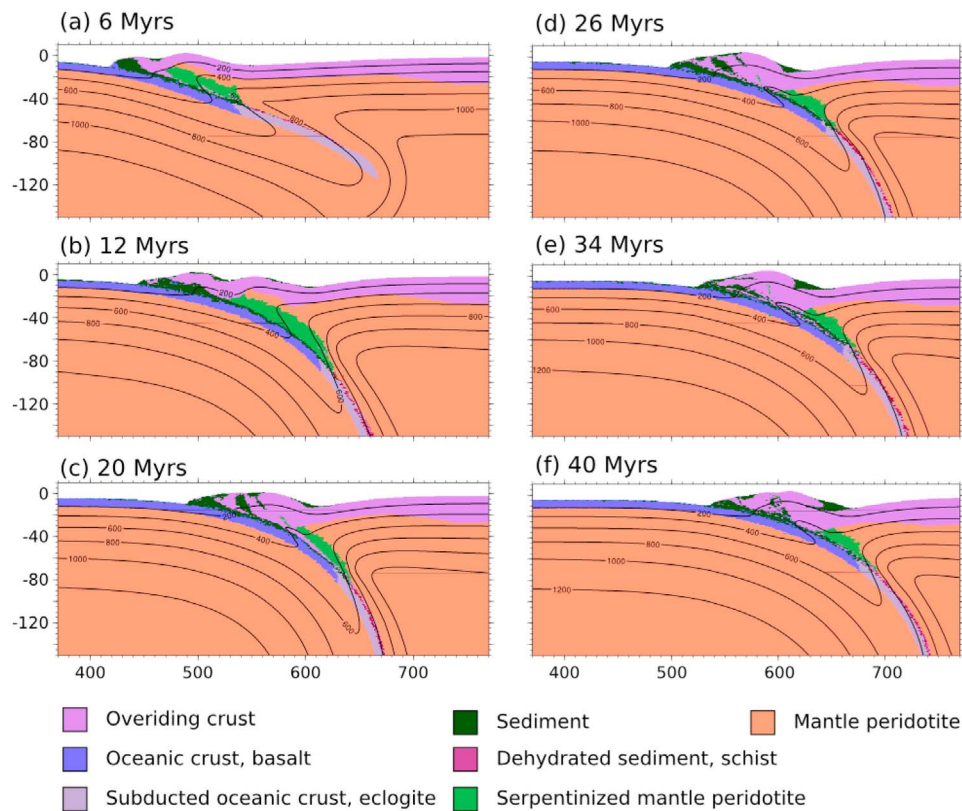
Figure 5. Case of $\phi = 3°$ and $H_{serp} = 20$ km. (a) Subduction initiation and buckling of the forearc; (b) trench advance and thickening, buckling of the forearc and slab steepening; (c) formation of the forearc prism; (d, e, f) the forearc prism structure and the slab interface have reached steady state.

contours, and we measured its dip angle θ and downdip width W. Both θ and W are obtained by measuring the linear length of the subduction interface since the interface has a small curvature. We estimate that the uncertainty on the measurement of θ is about $\pm1°$ for the low friction cases and $\pm4°$ for the high friction cases and the uncertainty on the measurement of W is 5–10 km. We first present the result of two end-member cases, one for which the friction angle ϕ of sediments and serpentinized peridotite at the interface is 3° (low friction) and another one where the friction angle is 15° (high friction). We then analyze the whole parameter space and compare our results with observational studies.

4.1. Low Friction Model

[22] The first case we examine has a low friction angle $\phi = 3°$ in the sediments and serpentinite that occupies the subduction interface and a serpentinite thickness H_{serp} of 20 km above the downgoing plate in the mantle wedge. As we start horizontal shortening, subduction initiates at the pre-existing weak zone. After 6 Myr, a slab with a length of

250 km of thin oceanic crust has underthrusted the overriding forearc to a depth of about 100 km in the mantle (Figure 5a). Temperature and pressure in the slab increase as it is sinking deeper into the mantle. Our assumed dehydration and eclogite transformation in the oceanic crust (equation (3)) takes place at depths of about 50 km. At the same time, a layer of serpentinized peridotite forms in the mantle wedge. Owing to their low friction, the incoming sediments deform easily when they enter the subduction zone. Most of deformed sediment is accreted in front of the forearc but small amounts are carried along the subduction interface (Figure 5b). When the subducted sediments reach a temperature and a pressure adequate for phase transformation they are transformed into schists and transported deep into the mantle.

[23] As the subduction zone develops, the forearc region of the overriding plate buckles first at 6 Myr (Figure 5a) and then thickens at 20 Myr (Figure 5c). This thick forearc is weak and continues to deform (Figures 5b–5d), to eventually rise above sea level. From 6 to 20 Myrs, the trench migrates toward the upper plate rapidly as material from the upper plate
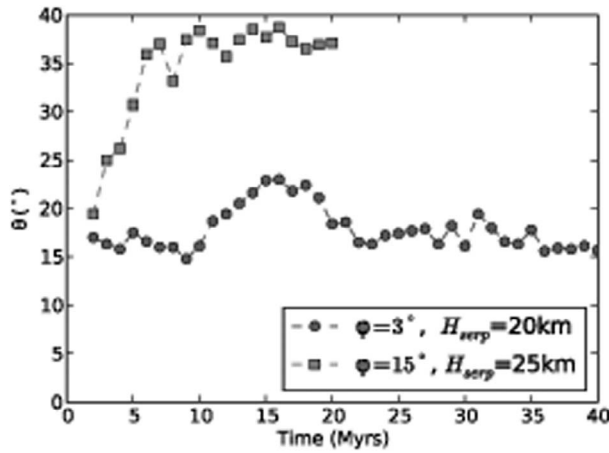
Figure 6. Evolution of the dip angle θ as a function of time. When the interface is weak (blue circles) the subduction interface dip reaches a steady state after 20 Myrs of bucking and thickening of the forearc by accretion of sediments of upper plate material. When the slab interface is strong (green squares) the system reaches a steady steep interface dip after 10 Myrs.

and incoming sediments thicken into a prism whose geometry reaches a steady state. Though a large fraction of the prism mass is derived from the ancient forearc, the shape of the forearc when stabilized (Figures 5c–5f) is similar to what is predicted by critical wedge theory [*Davis et al.*, 1983]. After 22 Myr, the geometry of the subduction zone

reaches equilibrium (Figures 5d–5f), with a stable trench location and a dip angle θ that varies little from 16° (Figure 6, blue line). The initial variation in slab dip is likely the result from changes in forces at the slab interface during the development of the forearc prism.
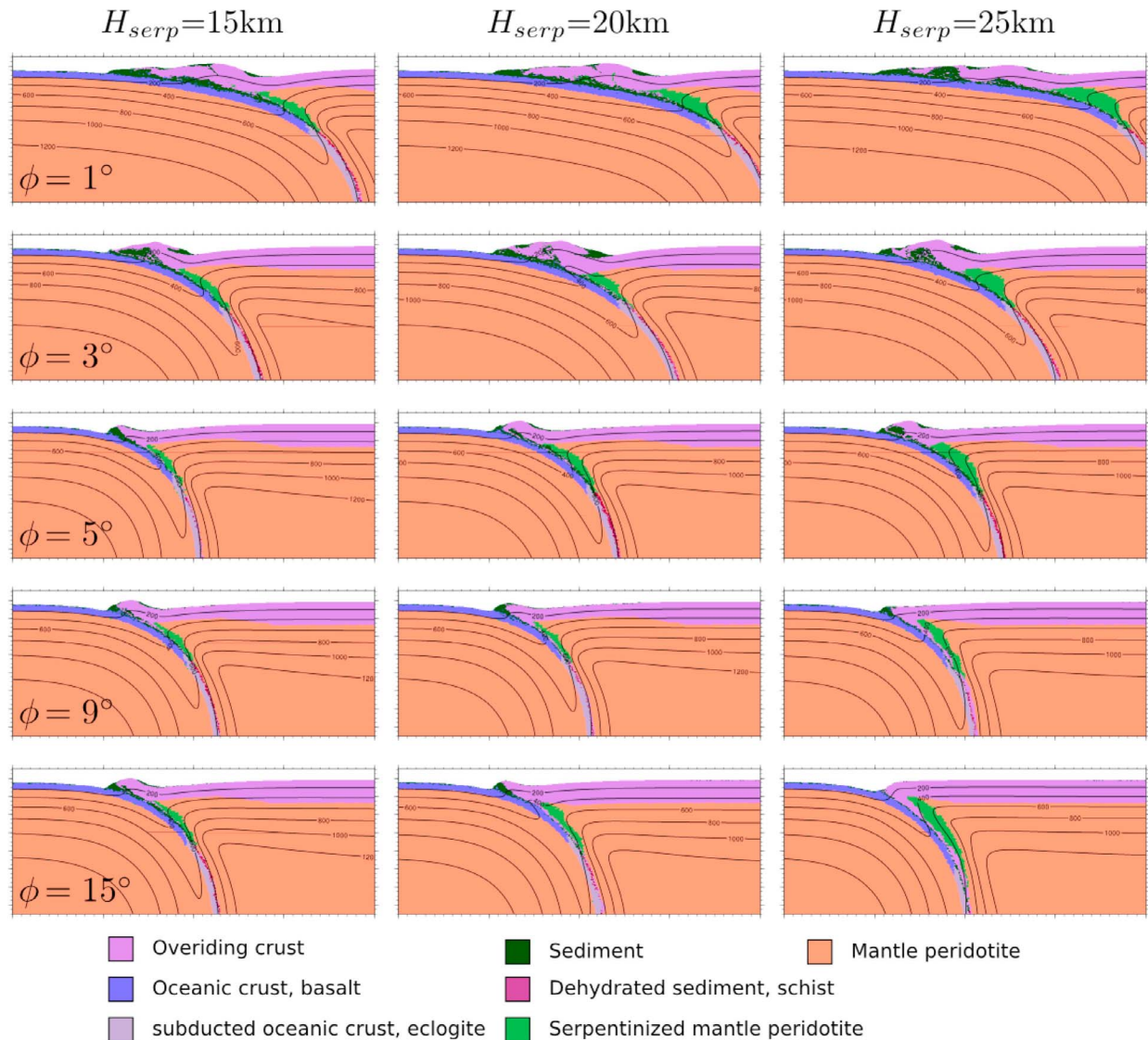
[24] The subduction interface has a shallow dip angle and large downdip width between 100° and 400°C. At 40 Myr, the basement depth at the trench is relatively shallow (≈11 km below sea level), compared with other cases, while the forearc basin is deep and the slab dip is about 16°. Even though the depth to basement at the trench is rather deep in the model (11 km), it is not in disagreement with observations of basement depth at subduction zones (see Figure 2b).

4.2. High Friction Model

[25] The second end-member case has a high friction angle $\phi = 15°$ for both the sediments and serpentinite. In addition, the zone of serpentinized peridotite at the base of the mantle wedge H_{serp} is 25 km thick in the model (Figure 7). The model develops a subduction zone just as in the low friction case (Figure 5), though the dip angle is steeper (~30°) and the section of the interface between 100°C and 400°C is not as wide. The geometry of the subduction reaches equilibrium quickly after 10 Myrs (Figure 6, green line). After 10 Myrs, slab
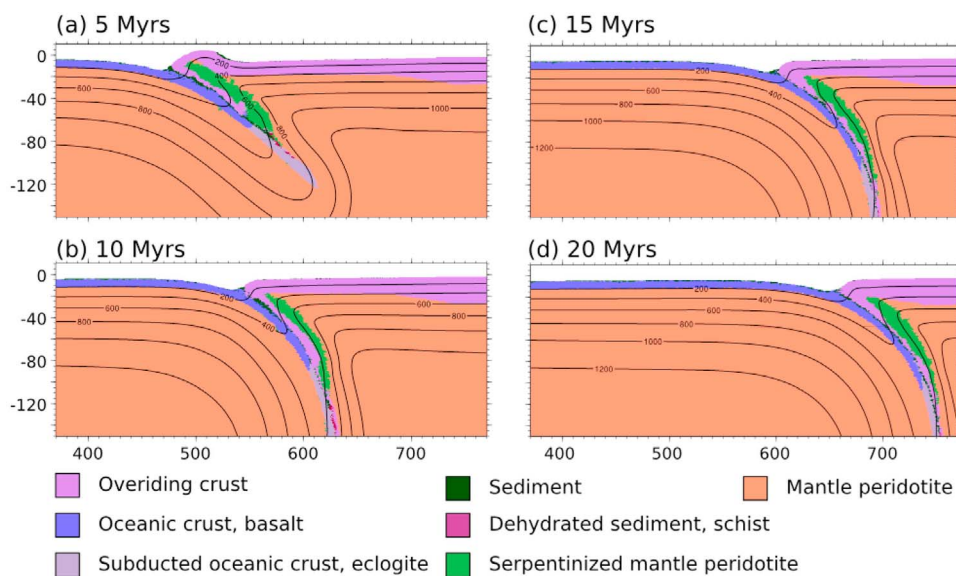
Figure 7. Case of $\phi = 15°$ and $H_{serp} = 25$ km. (a) Subduction initiation and buckling of the forearc; (b) the trench advances and the forearc is dragged into the subduction as the slab interface steepens; (c, d) the trench moves toward the upper plate as subduction erosion continuously erodes the upper plate. During that time the forearc structure and the interface dip are constant.

$H_{serp}=15$km $H_{serp}=20$km $H_{serp}=25$km

$\phi=1°$

$\phi=3°$

$\phi=5°$

$\phi=9°$

$\phi=15°$

- ▮ Overriding crust
- ▮ Oceanic crust, basalt
- ▮ subducted oceanic crust, eclogite
- ▮ Sediment
- ▮ Dehydrated sediment, schist
- ▮ Serpentinized mantle peridotite
- ▮ Mantle peridotite

Figure 8. Summary of all subduction models. The trenches are aligned in the plots. From top to bottom the friction ϕ at the subduction interface increases from 1° to 15°. From left to right the thickness of the serpentinized mantle wedge layer H_{serp} increases from 15 to 25 km. The calculations show a systematic steepening of the subduction interface as a function of friction angle.

dip is constant at about 37°. After 20 Myrs, the trench and the slab are too close to the right boundary (at 960 km) and their motion become strongly influenced by the boundary conditions. We therefore terminate the model calculation at 20 Myr.

[26] Since the friction angle of the sediments is the same as that of the weakened oceanic crust (15°), the interface is not lubricated by weak material. Therefore, there is strong resistance to motion at the subduction interface. Most of the sediments are carried down into the mantle by the slab, while little sediment is accreted. The frontal part of the

overriding plate is continuously stressed and dragged down with the subducting plate. There is no forearc high and the basement at the trench is very deep (~15 km below sea level). No forearc basin forms since the upper plate does not thicken. Because the overriding plate is losing mass by tectonic erosion, the trench moves rapidly toward the upper plate.

4.3. Parameter Space

[27] The two models with low and high friction angle ϕ at the plate boundary represent end-member cases that resemble an accretionary margin and an
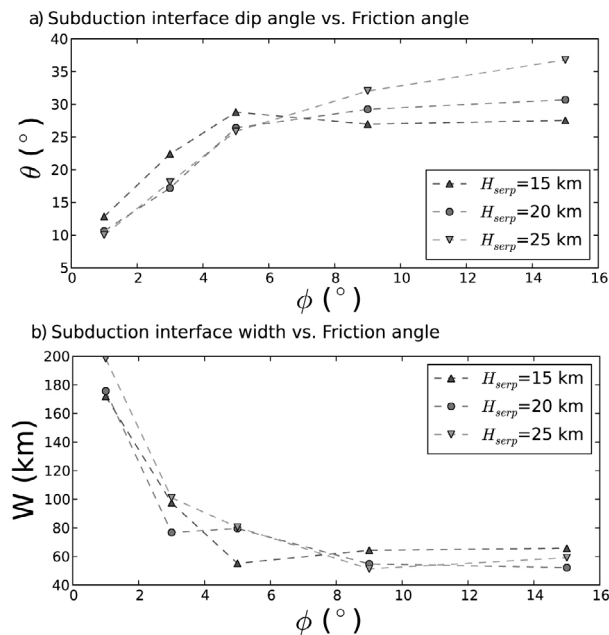
Figure 9. (a) Variation of dip angle θ as a function friction angle ϕ at the subduction interface. (b) Variation of seismogenic zone width W as a function of friction angle ϕ.

erosive margin, respectively [*von Huene and Scholl*, 1991; *Clift and Vannucchi*, 2004]. We now further explore the variables ϕ and H_{serp} with 15 experimental runs (Figure 8). When ϕ is smaller than 3°, we find that the convergent margins are accretionary. The characteristics are shallow subduction dip, shallow trench, broad forearc high, and deep forearc basin. Conversely, when ϕ is greater than 9° and H_{serp} is thicker than 25 km, an erosive convergent margin develops in our model, characterized by steep subduction interface dip, a deep trench, no forearc high, and no forearc basin (Figure 8). When ϕ is intermediate to large (between 5° to 15°) and H_{serp} is thin to intermediate (between 15 to 20 km), the resulting convergent margin has attributes that fall between the two end-member cases. In these models the subduction dip is intermediate, the forearc high is small and narrow, and the forearc basin is shallow (Figure 8). Although our numerical method simulates erosion and sedimentation, we may underestimate the effect of such complex 3-D surficial processes. If we could better account for sediment transport and deposition, we expect that most of the forearc high would be eroded if above the sea level, and the forearc basin and the trench would be filled with more sediments.

[28] We find that the friction angle ϕ correlates strongly with the dip θ, and with the inverse of the downdip width W of the seismogenic segment (Figure 9). When the friction angle ϕ of the sediment and serpentinized mantle is low, the dip angle θ of the subduction interface is low, and W is large. Conversely, strong sediments and serpentinized mantle (large ϕ) will steepen the subduction interface (Figure 9a) and shorten W (Figure 9b).

[29] The effect of the mantle wedge serpentinite thickness H_{serp} is more subtle. When ϕ is large (>5°), a thicker serpentinized layer at the base of the mantle wedge will increase the dip angle θ (Figures 8 and 9a). In an erosive margin, the subducting plate drags both the forearc prism and parts of the mantle wedge into the deeper mantle. The resistances of the forearc prism and of the mantle wedge act together to balance the drag. When the serpentinized mantle layer is thick, the mantle wedge becomes weak. As a result, the forearc prism contributes most to the resistance. In other words, most of the drag is acting on the forearc prism and causes a steeper dip angle θ and stronger subduction erosion.

[30] Finally, the modeled temperature structure at the interface is colder for accretionary–type models than for erosive-type models (Figure 8). For a low friction coefficient at the plate interface, the shallow subduction dip maintains the interface at shallow depth and low temperatures, keeping it relatively cold. Consequently, the width of seismogenic segment is significantly longer in the low friction case (Figure 9b). For erosional margins the steep dip brings the subduction interface into a zone of higher temperatures. Our results (Figure 9b) show that when ϕ is greater than 5° the width is mostly independent on the strength of the subduction interface. However, it is nonlinearly decreasing from 200 km to 60 km when ϕ increases from 1° to 5°.

5. Discussion

5.1. Possible Range of Friction Angle at Plate Interface

[31] We presented a suite of 15 models of subduction to investigate the role of plate coupling at lithospheric and mantle wedge depths. We varied the friction between the two plates by adjusting the friction angle in both the sediments and serpentinite. These two materials may both be present at the plate boundary, either by sediment subduction or hydration of the mantle wedge. Our models show there is a strong correlation of subduction dip and friction angle in our models (Figure 9a). Some earlier geodynamic modeling studies [*van Keken*

et al., 2002; *Conder*, 2005; *Wada et al.*, 2008] concluded that a thin weak layer on the plate interface is necessary to obtain a realistic temperature structure in the mantle wedge, and to match heat flow profiles across the convergent margin at the Earth's surface. There is some geophysical evidence for such a thin, weak plate boundary beneath the forearc [*Audet et al.*, 2009; *Van Avendonk et al.*, 2010], but such observations do not rule out the possibility that some subduction zones have a strong plate interface. A large number of subduction zones have a seismogenic zone dip angle $\theta > 20°$ (Figure 2) suggests that the friction angle ϕ is often significantly larger than 1°.

[32] A surprising outcome of our modeling is that subduction can be maintained with a wide range of friction angles ϕ, from 1° to 15°. For larger friction angles we see changes in the nature of the plate boundary in our numerical models. Subduction is steady even when $\phi > 8°$, but as ϕ increases further it is accompanied with more subduction erosion. We expect that if the interface frictional strength exceeds the strength of the weakened lithosphere ($\phi = 15°$ in our model) the lower plates will deform and subduction will stall. In that case another subduction zone usually forms elsewhere on the lower plate. Our model does not provide a minimum value for the strength of the subduction interface, so the friction angle can be as low as 0.1°, which would be in agreement with other numerical experiments of subduction [e.g., *Gurnis et al.*, 2004]. However, the large range of observed interface dip θ (Figure 2a) shows that the strength of the subduction interface may vary greatly, although other processes, such as the coupling by motion of the overriding plate [e.g., *van Hunen et al.*, 2000], would also affect the interface dip, and the range of possible friction angle variation at the subduction interface can be smaller than the range we have explored.

5.2. Subduction Erosion

[33] Subduction erosion is the collective name of all geological processes that lead to the removal and subduction of forearc rock at a convergent margin [e.g., *von Huene and Scholl*, 1991]. Two different mechanisms for subduction erosion that have often been invoked are "basal erosion," where crustal rocks are shaved off the forearc at the contact with the downgoing ocean crust, and "frontal erosion," where oversteepening of the inner trench wall leads to gravitational collapse and subduction of forearc rocks [*von Huene and Lallemand*, 1990]. In both cases, subduction erosion is enhanced by

the underthrusting of seafloor with ridges and plateaus. For example, the tip of the forearc may break off when it is raised and dropped by the passing of a subducting seamount [e.g., *Ballance et al.*, 1989]. Alternatively, seamounts that pierce through the sediment cover may increase the friction at the base of the forearc [*Clift et al.*, 2003].

[34] Our numerical models with friction angles ϕ of 1°–5° are representative of convergent margins that are well lubricated with sediments. Subduction erosion is absent in these cases as a result. On the other hand, a high value of ϕ, will increase the amount of subduction erosion substantially (Figure 8). Our models show that the friction angle ϕ of the sediments and the serpentine layer and the thickness of the serpentinized layer H_{serp} control whether a margin becomes accretionary or erosive. In the case of small ϕ, sediments accrete in wedges in front of the overriding plate, and the subduction interface is shallow. Conversely, for large ϕ and large H_{serp}, the convergent margin is erosive with little sediment accumulation at the plate boundary, and the subduction interface is steep. In addition, as explained by critical wedge theory [*Dahlen et al.*, 1984], the sediments with a small friction angle ϕ lead to a shallow and wide wedge, and shallow dipping plate interface, while stronger sediments give rise to a steeper plate boundary.

[35] One interpretation of the role of ϕ in the development of accretionary and erosive margins may consider the effect of seafloor roughness. In the case that sediment thickness is small and/or the seafloor is rough, basement highs on the downgoing plate will be strongly coupled against the overriding plate. Such a margin would be erosive [*Scholl and von Huene*, 2009]. Subduction of rough seafloor leads to tectonic erosion and diminishing of the forearc. Several compilation studies indicate that subduction erosion takes place at the majority of convergent margins on Earth, and preferentially near deep-sea trenches with thin sediment cover [*Clift and Vannucchi*, 2004; *Scholl and von Huene*, 2009; *Stern and Scholl*, 2010]. Seafloor relief that is produced on the flanks of slow-spreading mid-ocean ridges is between 100 m and 300 m high on average, while the fast spreading ridges of the Pacific produce relief that mostly varies between 40 m and 100 m [*Goff*, 1991]. The abyssal hill fabric of the world's ocean basins is therefore often lower than the sediment thickness encountered at trenches (Figure 2). However, when oceanic plates bend into deep-sea trenches, normal faults are reactivated [*Masson*, 1991] which increases seafloor roughness. In addition, dewatering and compaction
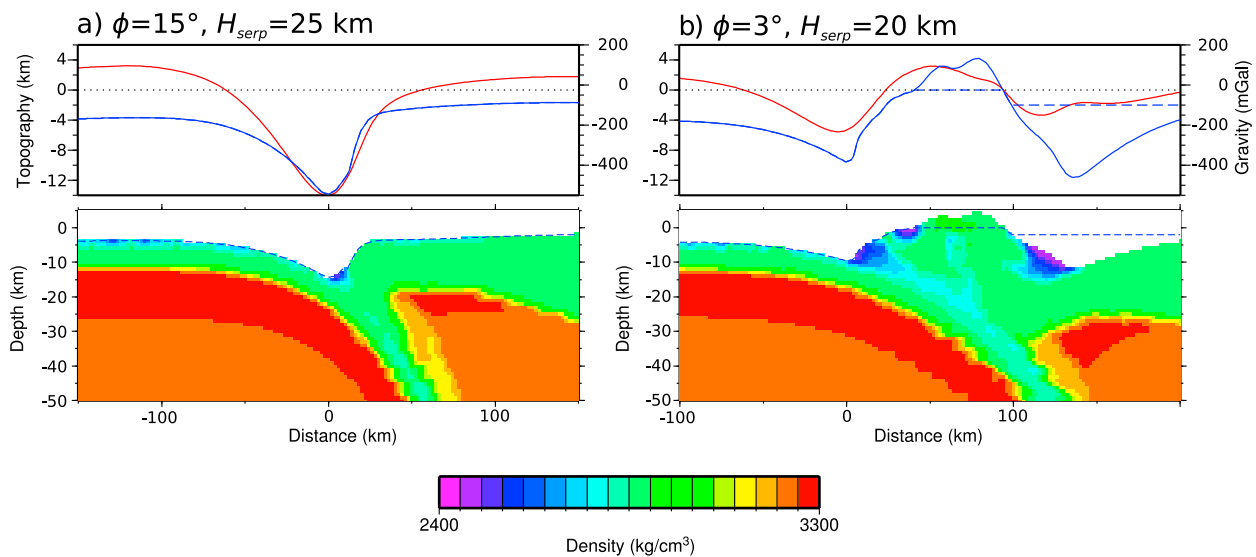
Figure 10. (a) Example of a high-friction model, with $\phi = 15°$ and $H_{serp} = 25$ km. (b) Example of a low-friction model, with $\phi = 3°$ and $H_{serp} = 20$ km. The upper panels show the model topography (solid blue line), the topography with post-processed erosion and sedimentation (dashed blue line), the sea level (dotted line) and the free-air gravity anomaly (red line). The lower panels show the density variation.

of subducting sediments beneath the prism [*Shipley and Moore*, 1986] will decrease the sediment thickness and increase coupling between the underlying seafloor ridges and scarps and the overlying forearc and mantle wedge.

5.3. Lithospheric Structure

[36] Since our numerical investigation aims to account for deformation on the scale of tectonic plates, we expect to find some resemblance between the distribution of crustal and mantle rock types in our models and the lithospheric structure of true subduction zones. However, our method does not include the effect of mantle melting and arc volcanism. The high, steep volcanic arcs and adjacent aprons of volcanoclastic sediments represent a large volume of young crustal material [e.g., *Scholl and von Huene*, 2007] that is not represented in our models. Collisional orogens form an additional source of sediments that often feed into convergent margins. In our study we treat the surface erosion process as diffusion of topography only. To model erosional processes accurately would require a more complete description of transport processes [*Willett*, 1999]. We chose to limit the effect of erosion and sedimentation in our model and to use a simple diffusion scheme [*Jordan and Flemings*, 1991] that results in a few mm/yr of material transport. When comparing our models with seismic reflection profiles across volcanic arcs [e.g., *von Huene et al.*, 1998], there is a clear deficiency

of sediments in the forearc basins and trenches in our models.

[37] To compute the free-air gravity anomaly from the mass distribution of our models and compare it to observations (Figure 10) we must account for the effects of erosion and sedimentation, which are much larger in nature than in our models. To remedy this limitation of our method, we post-process the surface topography in the model before computing the free-air gravity anomaly. The forearc high is completely eroded to sea level, and the forearc basins are filled with additional sediments up to 2 km below sea level (Figure 10, dashed blue lines). These assumptions seem to match the observations (Figure 1) relatively well. We compute the free-air gravity and topography profiles for two end-member models to compare with the observed profiles from Sumatra and central Aleutians (Figure 1).

[38] The end-member model of a convergent margin with high friction ($\phi = 15°$ and $H_{serp} = 25$ km) results in a gravity low at the trench adjacent to a high reaching approximately 100 mGal on the forearc (Figure 10a, red line). Owing to the large depth to basement (15 km), the difference in gravity anomaly between the trench and forearc is about 500 mGal, similar to that of the Aleutian margin (~400 mGal, Figure 1a). On the other hand, the modeled depth to basement at the trench is relatively high for a subduction zone. On erosive margins, such as central Aleutians (Figure 1a), we

generally observe a steep subduction interface, a deep trench, and no forearc high or forearc basin. These features are well reproduced by the high-friction model (Figure 10a).

[39] Our end-member model for a low-friction ($\phi = 3°$ and $H_{serp} = 20$ km) convergent margin develops a smaller subduction dip angle and a shallower trench (Figure 10b). After correction for erosion and sedimentation we obtain a negative gravity anomaly in the trench, a positive high at the forearc and a second negative anomaly corresponding to a forearc basin. The modeled gravity peak-to-peak amplitude is approximately 300 mGal, with a depth to basement at the trench of 11 km. The seismic observations of the accretionary convergent margin in Sumatra (Figure 1) show a peak-to-peak free-air gravity amplitude of 200 mGal, with a depth to basement at the trench of 10 km. The positive gravity anomaly of 100 mGal in the forearc region, due to the thickened crustal material, and the negative anomaly of −150 mGal in the forearc basin region match the gravity signature of Sumatra (Figure 1b).

5.4. Comparison With Past Numerical Studies

[40] Several past numerical studies assume a very low values for the friction angle (<5°) at the subduction interface [*Hassani et al.*, 1997; *Hall et al.*, 2003; *Gurnis et al.*, 2004; *Sobolev and Babeyko*, 2005; *Gorczyk et al.*, 2007; *Kaus et al.*, 2008; *Faccenda et al.*, 2009]. All of these models unsurprisingly have very shallow dipping subduction interface above 50 km depth, which is consistent with our model results. By incorporating serpentinization in the mantle wedge and the plastic strain weakening of the lithosphere, our numerical models can attain stable subduction at larger friction angle (up to 15°) and, therefore, have wider range of subduction dips.

[41] Our models show that the frictional strength of subducting interface will control whether a convergent margin is erosive or accretionary. This result is similar with the model of *van Dinther et al.* [2012], where weak sediments (low ϕ) are easily scraped from the incoming plate, and strong sediments resist deformation and are entrained in the deeper mantle, although they use very small friction coefficients (0–0.05) for the sediments.

[42] *Gerya and Meilick* [2011] have already shown numerically that the plate interface controls the lithospheric structure at subduction zones. Instead of changing friction angle, they changed the ratio of pore fluid pressure to lithostatic pressure to control the effective friction coefficient on the plate interface. They show the same relationship between the strength of the subduction interface and the type of subduction (accretionary versus erosional) as we have shown in this paper. Moreover, they also show that erosional margins tend to have a steep dip while accretionary types have a shallow subduction interface, large frontal wedge, and forearc basin. However, the differences in the treatment of melting and sediment metamorphism lead to minor differences in the model outcomes. Our models do not include melting and do not have magmatism and backarc spreading as a result. Additionally, in our models the sediment compaction prograde schist metamorphism allow sediments to subduct into the deep mantle, so sediments do not form cold plumes in the mantle wedge.

5.5. Seismogenic Potential

[43] It has been noted that the trench-parallel (along-strike) gravity variation correlates positively with the trench-parallel topography anomaly and negatively with the occurrence of great earthquakes [*Song and Simons*, 2003]. The majority of the seismic moment released by great earthquakes occurs beneath the prominent gravity low outlining the deep-sea terrace [*Wells et al.*, 2003]. The interpretation of these correlations is that strong coupling along subduction interface will drag down the forearc of the overriding plate, which causes the gravity and topography anomalies, and could store more elastic energy to be released during a great earthquake [*Song and Simons*, 2003]. The traditional view suggests that strong coupling along subduction interface requires high friction coefficient [*Cattin et al.*, 1997]. However, the results of this study suggest that regions with positive forearc topography and gravity anomalies should have low frictional strength. In fact, subduction zones with large forearc basins, such as Sumatra, eastern Alaska, Cascadia, and southern Chile, all have thicker sediment covers than the neighboring subduction zones (Figure 2).

[44] Although it seems counter-intuitive, low friction subduction interface actually promotes coupling of the upper and lower plates. Coupling is promoted in the low friction case because the development of a shallow and long subduction interface can prolong frictional contact between the upper and lower plates over a widening area. Although the frictional traction is low, integrated over the longer length of the subduction interface,

the total coupling will be greater than that of steeply dipping subduction zones.

[45] Our numerical models also suggest that the downdip width W of the seismogenic zone is larger in the case of low friction than in a subduction zone with high friction. The seismic moment of an earthquake may be expressed as:

$$M = \nu A_R d, \qquad (5)$$

where ν is the elastic shear modulus, A_R is the rupture area for an earthquake and d the amount of slip occurring on the ruptured area. A_R is clearly related to the maximum downdip and along-strike rupture lengths of the earthquake. It is conceivable that, in the case of a very large earthquake, the whole downdip length W is ruptured. On the other hand, it has been suggested that seafloor roughness can form barriers that limit the along-strike propagation of large earthquakes [*Bilek et al.*, 2003; *Bilek*, 2007]. Sediment-rich subduction zones will have smooth interfaces that can rupture over large along-strike length in a single earthquake [*Ruff*, 1989]. Interestingly, four of the five largest earthquakes ever recorded (moment magnitude $M_w > 9$) happened on subduction zones with shallow dip angle ($\theta < 15°$, which represent 30% of global subduction zones by length), where the predicted interface strength is low. The 2004 Sumatra and 2011 Tohoku earthquakes both ruptured a downdip length over 150 km and had a very shallow dip ($\theta \approx 10°$) [*Ammon et al.*, 2005; *Simons et al.*, 2011]. It is therefore conceivable that megathrust earthquakes happen preferentially on sediment-rich subduction zones, where the friction is low and the dip is shallow.

6. Conclusions

[46] We presented a suite of 15 thermomechanical models of the lithospheric structure of subduction zones (Figure 8). We varied material properties to show the effect of friction angle of sediments and serpentinite near the plate interface to understand the role of frictional coupling on the evolution of convergent margins. By imposing a fixed convergence velocity across a boundary between oceanic and continental lithosphere we can generate a subduction zone with stable geometry during 10 to 20 Myr (Figure 6). Our calculations show that a subduction zones with a small friction angle in its sediments and serpentinite ($\phi < 8°$) develop a weak, shallow-dipping megathrust, whereas a higher friction angle ($\phi > 8°$) will produce a plate interface

that dips no less than 15° beneath the forearc (Figure 9). Our numerical models (Figure 8) indicate that extremely low friction ($\phi < 1°$) on the subduction interface is not necessary to maintain subduction, if strain weakening in the subducting plate is included in the models. By imposing a fixed convergence velocity across a boundary between oceanic and continental lithosphere we can generate a subduction zone with stable geometry in 10 to 20 Myr (Figure 6). Our calculations show that a subduction zone with a small friction angle in its sediments and serpentinite ($\phi < 8°$) develop a weak, shallow-dipping megathrust, whereas a higher friction angle ($\phi > 8°$) will produce a plate interface that dips no less than 15° beneath the forearc (Figure 9). The wide range in numerical models (Figure 8) indicates that very low friction ($\phi < 5°$) on the subduction interface is not necessary to maintain subduction.

[47] Our calculations show that convergent margins with strong friction between the plates will develop a deep trench with a large negative gravity anomaly. These models develop neither a forearc high nor a forearc basin (Figure 10). Conversely, subduction zones with weak friction form a shallow trench, a broad forearc and an adjacent forearc basin. The shallow plate interface of weak subduction zones potentially creates a very wide coupled surface with long downdip and along-strike lengths that can rupture in a large earthquake. Our numerical models may provide an explanation why the largest earthquakes appear to happen at heavily sedimented subduction zones.

Acknowledgments

References

Abers, G. A. (2005), Seismic low-velocity layer at the top of subducting slabs: Observations, predictions, and systematics,

Phys. Earth Planet. Inter., *149*, 7–29, doi:10.1016/j.pepi.2004.10.002.

Ammon, C. J., et al. (2005), Rupture process of the 2004 Sumatra-Andaman Earthquake, *Science*, *308*, 1133–1139, doi:10.1126/science.1112260.

Audet, P., M. G. Bostock, N. I. Christensen, and S. M. Peacock (2009), Seismic evidence for overpressured subducted oceanic crust and megathrust fault sealing, *Nature*, *457*, 76–78, doi:10.1038/nature07650.

Ballance, P. F., D. W. Scholl, T. L. Vallier, A. J. Stevenson, H. Ryan, and R. H. Herzer (1989), Subduction of a late Cretaceous seamount of the Louisville ridge at the Tonga trench: A model of normal and accelerated tectonic erosion, *Tectonics*, *8*, 953–962, doi:10.1029/TC008i005p00953.

Bangs, N. L., T. H. Shipley, S. P. S. Gulick, G. F. Moore, S. Kuromoto, and Y. Nakamura (2004), Evolution of the Nankai Trough décollement from the trench into the seismogenic zone: Inferences from three-dimensional seismic reflection imaging, *Geology*, *32*, 273–276, doi:10.1130/G20211.2.

Bilek, S. L. (2007), Influence of subducting topography on earthquake rupture, in *The Seismogenic Zone of Subduction Thrust Faults*, edited by T. H. Dixon and J. C. Moore, pp. 123–146, Columbia Univ. Press, New York.

Bilek, S. L. (2010), The role of subduction erosion on seismicity, *Geology*, *38*, 479–480, doi:10.1130/focus052010.1.

Bilek, S. L., S. Y. Schwartz, and H. R. DeShon (2003), Control of seafloor roughness on earthquake rupture behavior, *Geology*, *31*, 455–458, doi:10.1130/0091-7613(2003)031<0455:COSROE>2.0.CO;2.

Blanpied, M. L., D. A. Lockner, and J. D. Byerlee (1995), Frictional slip of granite at hydrothermal conditions, *J. Geophys. Res.*, *100*, 13,045–13,064, doi:10.1029/95JB00862.

Buffett, B. A., and T. W. Becker (2012), Bending stress and dissipation in subducted lithosphere, *J. Geophys. Res.*, *117*, B05413, doi:10.1029/2012JB009205.

Byerlee, J. (1978), Friction of rocks, *Pure Appl. Geophys.*, *116*, 615–626, doi:10.1007/BF00876528.

Carlson, R. L., and D. J. Miller (2003), Mantle wedge water contents estimated from seismic velocities in partially serpentinized peridotites, *Geophys. Res. Lett.*, *30*(5), 1250, doi:10.1029/2002GL016600.

Cattin, R., H. Lyon-Caen, and J. Chéry (1997), Quantification of interplate coupling in subduction zones and forearc topography, *Geophys. Res. Lett.*, *24*, 1563–1566, doi:10.1029/97GL01550.

Chauhan, A. P. S., S. C. Singh, N. D. Hananto, H. Carton, F. Klingelhoefer, J.-X. Dessa, H. Permana, N. J. White, D. Graindorge, and the SumatraOBS Scientific Team (2009), Seismic imaging of forearc backthrusts at northern Sumatra subduction zone, *Geophys. J. Int.*, *179*, 1772–1780, doi:10.1111/j.1365-246X.2009.04378.x.

Chen, Y., and W. J. Morgan (1990), A nonlinear rheology model for mid-ocean ridge axis topography, *J. Geophys. Res.*, *95*, 17,583–17,604, doi:10.1029/JB095iB11p17583.

Clift, P. D., and P. Vannucchi (2004), Controls on tectonic accretion versus erosion in subduction zones: Implications for the origin and recycling of the continental crust, *Rev. Geophys.*, *42*, RG2001, doi:10.1029/2003RG000127.

Clift, P. D., I. Pecher, N. Kukowski, and A. Hampel (2003), Tectonic erosion of the Peruvian forearc, Lima Basin, by subduction and Nazca Ridge collision, *Tectonics*, *22*(3), 1023, doi:10.1029/2002TC001386.

Collettini, C., A. Niemeijer, C. Viti, and C. Marone (2009), Fault zone fabric and fault weakness, *Nature*, *462*, 907–910, doi:10.1038/nature08585.

Conder, J. A. (2005), A case for hot slab surface temperatures in numerical viscous flow models of subduction zones with an improved fault zone parameterization, *Phys. Earth Planet. Inter.*, *149*, 155–164, doi:10.1016/j.pepi.2004.08.018.

Cundall, P. A. (1989), Numerical experiments on localization in frictional materials, *Ingenieur Archiv*, *59*, 148–159, doi:10.1007/bf00538368.

Dahlen, F. A., J. Suppe, and D. Davis (1984), Mechanics of fold-and-thrust belts and accretionary wedges: Cohesive Coulomb theory, *J. Geophys. Res.*, *89*, 10,087–10,101, doi:10.1029/JB089iB12p10087.

Davis, D., J. Suppe, and F. A. Dahlen (1983), Mechanics of fold-and-thrust belts and accretionary wedges, *J. Geophys. Res.*, *88*, 1153–1172, doi:10.1029/JB088iB02p01153.

Escartín, J., G. Hirth, and B. Evans (2001), Strength of slightly serpentinized peridotites: Implications for the tectonics of oceanic lithosphere, *Geology*, *29*, 1023–1026, doi:10.1130/0091-7613(2001)029<1023:SOSSPI>2.0.CO;2.

Faccenda, M., T. V. Gerya, and L. Burlini (2009), Deep slab hydration induced by bending-related variations in tectonic pressure, *Nat. Geosci.*, *2*, 790–793, doi:10.1038/ngeo656.

Faulkner, D. R., T. M. Mitchell, J. Behnsen, T. Hirose, and T. Shimamoto (2011), Stuck in the mud? Earthquake nucleation and propagation through accretionary forearcs, *Geophys. Res. Lett.*, *38*, L18303, doi:10.1029/2011GL048552.

Gerya, T. V., and F. I. Meilick (2011), Geodynamic regimes of subduction under an active margin: Effects of rheological weakening by fluids and melts, *J. Metamorph. Geol.*, *29*, 7–31, doi:10.1111/j.1525-1314.2010.00904.x.

Goff, J. A. (1991), A global and regional stochastic analysis of near-ridge abyssal hill morphology, *J. Geophys. Res.*, *96*, 21,713–21,737, doi:10.1029/91JB02275.

Gorczyk, W., A. P. Willner, T. V. Gerya, J. A. D. Connolly, and J.-P. Burg (2007), Physical controls of magmatic productivity at Pacific-type convergent margins: Numerical modelling, *Phys. Earth Planet. Inter.*, *163*, 209–232, doi:10.1016/j.pepi.2007.05.010.

Gulick, S. P. S., J. A. Austin, L. C. McNeill, N. L. B. Bangs, K. M. Martin, T. J. Henstock, J. M. Bull, S. Dean, Y. S. Djajadihardja, and H. Permana (2011), Updip rupture of the 2004 Sumatra earthquake extended by thick indurated sediments, *Nat. Geosci.*, *4*, 453–456, doi:10.1038/ngeo1176.

Gurnis, M., C. Hall, and L. Lavier (2004), Evolving force balance during incipient subduction, *Geochem. Geophys. Geosyst.*, *5*, Q07001, doi:10.1029/2003GC000681.

Hacker, B. R. (1996), Eclogite formation and the rheology, buoyancy, seismicity, and H_2O content of oceanic crust, in *Subduction Top to Bottom*, *Geophys. Monogr. Ser.*, vol. 96, edited by E. Bebout et al., pp. 337–346, AGU, Washington, D. C., doi:10.1029/GM096p0337.

Hall, C. E., M. Gurnis, M. Sdrolias, L. L. Lavier, and R. D. Müller (2003), Catastrophic initiation of subduction following forced convergence across fracture zones, *Earth Planet. Sci. Lett.*, *212*, 15–30, doi:10.1016/S0012-821X(03)00242-5.

Handy, M. R. (1989), Deformation regimes and the rheological evolution of fault zones in the lithosphere: The effects of pressure, temperature, grainsize and time, *Tectonophysics*, *163*, 119–152, doi:10.1016/0040-1951(89)90122-4.

Hassani, R., D. Jongmans, and J. Chéry (1997), Study of plate deformation and stress in subduction processes using two-dimensional numerical models, *J. Geophys. Res.*, *102*, 17,951–17,965, doi:10.1029/97JB01354.

Heuret, A., S. Lallemand, F. Funiciello, C. Piromallo, and C. Faccenna (2011), Physical characteristics of subduction

interface type seismogenic zones revisited, *Geochem. Geophys. Geosyst.*, 12, Q01004, doi:10.1029/2010GC003230.

Heuret, A., C. P. Conrad, F. Funiciello, S. Lallemand, and L. Sandri (2012), Relation between subduction megathrust earthquakes, trench sediment thickness and upper plate strain, *Geophys. Res. Lett.*, 39, L05304, doi:10.1029/2011GL050712.

Hilairet, N., B. Reynard, Y. Wang, I. Daniel, S. Merkel, N. Nishiyama, and S. Petitgirard (2007), High-pressure creep of serpentine, interseismic deformation, and initiation of subduction, *Science*, 318, 1910–1913, doi:10.1126/science.1148494.

Holbrook, W. S., D. Lizarralde, S. McGeary, N. Bangs, and J. Diebold (1999), Structure and composition of the Aleutian island arc and implications for continental crustal growth, *Geology*, 27, 31–34, doi:10.1130/0091-7613(1999)027<0031:SACOTA>2.3.CO;2.

Hyndman, R. D., and S. M. Peacock (2003), Serpentinization of the forearc mantle, *Earth Planet. Sci. Lett.*, 212, 417–432, doi:10.1016/S0012-821X(03)00263-2.

Jarrard, R. D. (1986), Relations among subduction zone parameters, *Rev. Geophys.*, 24, 217–284, doi:10.1029/RG024i002p00217.

Jordan, T. E., and P. B. Flemings (1991), Large-scale stratigraphic architecture, eustatic variation, and unsteady tectonism: A theoretical evaluation, *J. Geophys. Res.*, 96, 6681–6699, doi:10.1029/90JB01399.

Kaus, B. J. P., C. Steedman, and T. W. Becker (2008), From passive continental margin to mountain belt: Insights from analytical and numerical models and application to Taiwan, *Phys. Earth Planet. Inter.*, 171, 235–251, doi:10.1016/j.pepi.2008.06.015.

Kirby, S. H., and A. K. Kronenberg (1987), Rheology of the lithosphere: Selected topics, *Rev. Geophys.*, 25, 1219–1244, doi:10.1029/RG025i006p01219.

Klingelhoefer, F., M. A. Gutscher, S. Ladage, J. X. Dessa, D. Graindorge, D. Franke, C. Andre, H. Permana, T. Yudistira, and A. Chauhan (2010), Limits of the seismogenic zone in the epicentral region of the 26 December 2004 great Sumatra-Andaman earthquake: Results from seismic refraction and wide-angle reflection surveys and thermal modeling, *J. Geophys. Res.*, 115, B01304, doi:10.1029/2009JB006569.

Kodaira, S., T. Iwasaki, T. Urabe, T. Kanazawa, F. Egloff, J. Makris, and H. Shimahura (1996), Crustal structure across the middle Ryukyu trench obtained from ocean bottom seismographic data, *Tectonophysics*, 263, 39–60, doi:10.1016/S0040-1951(96)00025-X.

Lallemand, S., A. Heuret, and D. Boutelier (2005), On the relationships between slab dip, back-arc stress, upper plate absolute motion, and crustal nature in subduction zones, *Geochem. Geophys. Geosyst.*, 6, Q09006, doi:10.1029/2005GC000917.

Lavier, L. L., W. R. Buck, and A. N. B. Poliakov (2000), Factors controlling normal fault offset in an ideal brittle layer, *J. Geophys. Res.*, 105, 23,431–23,442.

Lizarralde, D., W. S. Holbrook, S. McGeary, N. Bangs, and J. Diebold (2002), Crustal construction of a volcanic arc, wide-angle seismic results from the western Alaska Peninsula, *J. Geophys. Res.*, 107(B8), 2164, doi:10.1029/2001JB000230.

Lockner, D. A., C. Morrow, D. Moore, and S. Hickman (2011), Low strength of deep San Andreas fault gouge from SAFOD core, *Nature*, 472, 82–85, doi:10.1038/nature09927.

Masson, D. G. (1991), Fault patterns at outer trench walls, *Mar. Geophys. Res.*, 13, 209–225, doi:10.1007/BF00369150.

McIntosh, K. D., E. A. Silver, I. Ahmed, A. Berhorst, C. R. Ranero, R. K. Kelly, and E. R. Flueh (2007), The Nicaragua convergent margin: Seismic reflection imaging of the source

of a tsunami earthquake, in *The Seismogenic Zone of Subduction Thrust Faults*, edited by T. Dixon and J. C. Moore, pp. 257–287, Columbia Univ. Press, New York.

Moore, D. E., D. A. Lockner, M. Shengli, R. Summers, and J. D. Byerlee (1997), Strengths of serpentinite gouges at elevated temperatures, *J. Geophys. Res.*, 102, 14,787–14,801, doi:10.1029/97JB00995.

Moore, D. E., D. A. Lockner, H. Tanaka, and K. Iwata (2004), The coefficient of friction of chrysotile gouge at seismogenic depths, *Int. Geol. Rev.*, 46, 385–398, doi:10.2747/0020-6814.46.5.385.

Moore, J. C., and D. Saffer (2001), Updip limit of the seismogenic zone beneath the accretionary prism of southwest Japan: An effect of diagentic to low-grade metamorphic processes and increasing effective stress, *Geology*, 29, 183–186, doi:10.1130/0091-7613(2001)029<0183:ULOTSZ>2.0.CO;2.

Moore, J. C., et al. (1991), EDGE deep seismic reflection transect of the eastern Aleutian arc-trench layered lower crust reveals underplating and continental growth, *Geology*, 19, 420–424, doi:10.1130/0091-7613(1991)019<0420:EDSRTO>2.3.CO;2.

Moore, J. C., et al. (1995), Abnormal fluid pressures and fault-zone dilation in the Barbados accretionary prism: Evidence from logging while drilling, *Geology*, 23, 605–608, doi:10.1130/0091-7613(1995)023<0605:AFPAFZ>2.3.CO;2.

Nichols, G. T., P. J. Wyllie, and C. R. Stern (1994), Subduction zone melting of pelagic sediments constrained by melting experiments, *Nature*, 371, 785–788, doi:10.1038/371785a0.

Nikulin, A., V. Levin, and J. Park (2009), Receiver function study of the Cascadia megathrust: Evidence for localized serpentinization, *Geochem. Geophys. Geosyst.*, 10, Q07004, doi:10.1029/2009GC002376.

Oleskevich, D. A., R. D. Hyndman, and K. Wang (1999), The updip and downdip limits to great subduction earthquakes: Thermal and structural models of Cascadia, south Alaska, SW Japan, and Chile, *J. Geophys. Res.*, 104, 14,965–14,991 doi:10.1029/1999JB900060.

Pacheco, J. F., L. R. Sykes, and C. H. Scholz (1993), Nature of seismic coupling along simple plate boundaries of the subduction type, *J. Geophys. Res.*, 98, 14,133–14,159, doi:10.1029/93JB00349.

Peacock, S. M. (1993), The importance of blueschist eclogite dehydration reactions in subducting oceanic crust, *Geol. Soc. Am. Bull.*, 105, 684–694, doi:10.1130/0016-7606(1993)105<0684:TIOBED>2.3.CO;2.

Poliakov, A. N. B., P. A. Cundall, Y. Y. Podladchikov, and V. A. Lyakhovsky (1993), An explicit inertial method for the simulation of viscoelastic flow: An evaluation of elastic effects on diapiric flow in two-and three-layers models, in *Flow and Creep in the Solar System: Observations, Modeling and Theory*, vol. 391, pp. 175–195, Kluwer Acad., Dordrecht, Netherlands.

Ranalli, G. (1986), *Rheology of the Earth*, 366 pp., Allen & Unwin, Boston, Mass.

Ruff, L. J. (1989), Do trench sediments affect great earthquake occurrence in subduction zones?, *Pure Appl. Geophys.*, 129, 263–282, doi:10.1007/BF00874629.

Saffer, D. M., and C. Marone (2003), Comparison of smectite- and illite-rich gouge frictional properties: Application to the updip limit of the seismogenic zone along subduction megathrusts, *Earth Planet. Sci. Lett.*, 215, 219–235, doi:10.1016/S0012-821X(03)00424-2.

Saffer, D. M., D. A. Lockner, and A. McKiernan (2012), Effects of smectite to illite transformation on the frictional strength

and sliding stability of intact marine mudstones, *Geophys. Res. Lett.*, *39*, L11304, doi:10.1029/2012GL051761.

Sallarès, V., and C. R. Ranero (2005), Structure and tectonics of the erosional convergent margin off Antofagosta, north Chile (23°30′S), *J. Geophys. Res.*, *110*, B06101, doi:10.1029/2004JB003418.

Sandwell, D. T., and W. H. F. Smith (2009), Global marine gravity from retracked Geosat and ERS-1 altimetry: Ridge segmentation versus spreading rate, *J. Geophys. Res.*, *114*, B01411, doi:10.1029/2008JB006008.

Schmidt, M. W., and S. Poli (1998), Experimentally based water budgets for dehydrating slabs and consequences for arc magma generation, *Earth Planet. Sci. Lett.*, *163*, 361–379, doi:10.1016/S0012-821X(98)00142-3.

Scholl, D. W., and R. von Huene (2007), Crustal recycling at modern subduction zones applied to the past—Issues of growth and preservation of continental basement crust, mantle geochemistry, and supercontinent reconstruction, in *4-D Framework of Continental Crust*, edited by R. D. Hatcher Jr. et al., *Mem. Geol. Soc. Am.*, *200*, 9–32.

Scholl, D. W., and R. von Huene (2009), Implications of estimated magmatic additions and recycling losses at the subduction zones of accretionary (non-collisional) and collisional (suturing) orogens, in *Earth Accretionary Systems in Space and Time*, edited by P. A. Cawood and A. Kroner, *Geol. Soc. Spec. Publ.*, *318*, 105–125.

Schwartz, S. Y., and J. M. Rokosky (2007), Slow slip events and seismic tremor at circum-Pacific subduction zones, *Rev. Geophys.*, *45*, RG3004, doi:10.1029/2006RG000208.

Shipley, T., and G. Moore (1986), Sediment accretion, subduction, and dewatering at the base of the trench slope off Costa Rica: A seismic reflection view of the décollement, *J. Geophys. Res.*, *91*, 2019–2028, doi:10.1029/JB091iB02p02019.

Simons, M., et al. (2011), The 2011 magnitude 9.0 Tohoku-Oki Earthquake: Mosaicking the megathrust from seconds to centuries, *Science*, *332*, 1421–1425, doi:10.1126/science.1206731.

Smith, W. H. F., and D. T. Sandwell (1997), Global sea floor topography from satellite altimetry and ship depth soundings, *Science*, *277*, 1956–1962, doi:10.1126/science.277.5334.1956.

Sobolev, S. V., and A. Y. Babeyko (2005), What drives orogeny in the Andes?, *Geology*, *33*, 617–620, doi:10.1130/G21557.1.

Sodoudi, F., X. Yuan, G. Asch, and R. Kind (2011), High-resolution image of the geometry and thickness of the subducting Nazca lithosphere beneath northern Chile, *J. Geophys. Res.*, *116*, B04302, doi:10.1029/2010JB007829.

Song, T. R. A., and M. Simons (2003), Large trench-parallel gravity variations predict seismogenic behavior in subduction zones, *Science*, *301*, 630–633, doi:10.1126/science.1085557.

Stern, R. J., and D. W. Scholl (2010), Yin and yang of continental crust creation and destruction by plate tectonic processes, *Int. Geol. Rev.*, *52*, 1–31, doi:10.1080/00206810903332322.

Syracuse, E. M., G. A. Abers, K. Fischer, L. MacKenzie, C. Rychert, M. Protti, V. González, and W. Strauch (2008), Seismic tomography and earthquake locations in the Nicaraguan and Costa Rican upper mantle, *Geochem. Geophys. Geosyst.*, *9*, Q07S08, doi:10.1029/2008GC001963.

Tibi, R., D. A. Wiens, and X. H. Yuan (2008), Seismic evidence for widespread serpentinized forearc mantle along the Mariana convergence margin, *Geophys. Res. Lett.*, *35*, L13303, doi:10.1029/2008GL034163.

Ulmer, P., and V. Trommsdorff (1995), Serpentine stability to mantle depths and subduction-related magmatism, *Science*, *268*, 858–861, doi:10.1126/science.268.5212.858.

Van Avendonk, H. J. A., W. S. Holbrook, D. Lizarralde, M. M. Mora, S. Harder, A. D. Bullock, G. E. Alvarado, and C. J.

Ramírez (2010), Seismic evidence for fluids in fault zones on top of the subducting Cocos plate beneath Costa Rica, *Geophys. J. Int.*, *181*, 997–1016, doi:10.1111/j.1365-246X.2010.04552.x.

Van Avendonk, H. J. A., W. S. Holbrook, D. Lizarralde, and P. Denyer (2011), Structure and serpentinization of the subducting Cocos plate offshore Nicaragua and Costa Rica, *Geochem. Geophys. Geosyst.*, *12*, Q06009, doi:10.1029/2011GC003592.

van Dinther, Y., G. Morra, F. Funiciello, F. Rossetti, and C. Faccenna (2012), Exhumation and subduction erosion in orogenic wedges: Insights from numerical models, *Geochem. Geophys. Geosyst.*, *13*, Q06003, doi:10.1029/2011GC004011.

van Hunen, J., A. P. van den Berg, and N. J. Vlaar (2000), A thermo-mechanical model of horizontal subduction below an overriding plate, *Earth Planet. Sci. Lett.*, *182*, 157–169, doi:10.1016/S0012-821X(00)00240-5.

van Keken, P. E., B. Kiefer, and S. M. Peacock (2002), High-resolution models of subduction zones: Implications for mineral dehydration reactions and the transport of water into the deep mantle, *Geochem. Geophys. Geosyst.*, *3*(10), 1056, doi:10.1029/2001GC000256.

von Huene, R., and S. Lallemand (1990), Tectonic erosion along the Japan and Peru convergent margins, *Geol. Soc. Am. Bull.*, *102*, 704–720, doi:10.1130/0016-7606(1990)102<0704:TEATJA>2.3.CO;2.

von Huene, R., and C. R. Ranero (2009), Neogene collision and deformation of convergent margins along the backbone of the Americas, in *Backbone of the Americas: Shallow Subduction, Plateau Uplift, and Ridge and Terrane Collision*, edited by S. Mahlburg Kay, V. A. Ramos, and W. R. Dickinson, *Mem. Geol. Soc. Am.*, *204*, 67–83.

von Huene, R., and D. W. Scholl (1991), Observations at convergent margins concerning sediment subduction, subduction erosion, and the growth of continental crust, *Rev. Geophys.*, *29*, 279–316, doi:10.1029/91RG00969.

von Huene, R., and D. W. Scholl (1993), The return of sialic material to the mantle indicated by terrigeneous material subducted at convergent margins, *Tectonophysics*, *219*, 163–175, doi:10.1016/0040-1951(93)90294-T.

von Huene, R., D. Klaeschen, M. Gutscher, and J. Fruehn (1998), Mass and fluid flux during accretion at the Alaskan margin, *Geol. Soc. Am. Bull.*, *110*, 468–482, doi:10.1130/0016-7606(1998)110<0468:MAFFDA>2.3.CO;2.

Wada, I., K. Wang, J. He, and R. D. Hyndman (2008), Weakening of the subduction interface and its effects on surface heat flow, slab dehydration, and mantle wedge serpentinization, *J. Geophys. Res.*, *113*, B04402, doi:10.1029/2007JB005190.

Wells, R. E., R. J. Blakely, Y. Sugiyama, D. W. Scholl, and P. A. Dinterman (2003), Basin-centered asperities in great subduction zone earthquakes: A link between slip, subsidence, and subduction erosion?, *J. Geophys. Res.*, *108*(B10), 2507, doi:10.1029/2002JB002072.

Willett, S. D. (1999), Orogeny and orography: The effects of erosion on the structure of mountain belts, *J. Geophys. Res.*, *104*, 28,957–28,981, doi:10.1029/1999JB900248.

Worthington, L. L., S. P. S. Gulick, and T. L. Pavlis (2010), Coupled stratigraphic and structural evolution of a glaciated orogenic wedge, offshore St. Elias orogen, Alaska, *Tectonics*, *29*, TC6013, doi:10.1029/2010TC002723.

Yamamoto, Y., R. Hino, and M. Shinohara (2011), Mantle wedge structure in the Miyagi Prefecture forearc region, central northeastern Japan arc, and its relation to corner-flow pattern and interplate coupling, *J. Geophys. Res.*, *116*, B10310, doi:10.1029/2011JB008470.